

Fabrication of helix-fiber composites with mechanically coupled core-wrapping for programmable properties

Dan Li^{1,3}, Zhiwei Zhu^{1,3}, Ziyu Zhao¹, Yuan Ji¹, Xuewei Fu¹ [✉], Zunfeng Liu² [✉], Wei Yang¹ [✉] & Yu Wang¹ [✉]

Helix-fiber composites (HFCs), which involve wrapping a material around a flexible core, are of interest for intelligent stretchable functional materials or devices. Here, we reveal that mechanical coupling between the core and wrapping plays a critical role in controlling the structure and mechanical properties. Our results show that the mechanical properties of the HFC can be programmed by precisely tuning the mechanical coupling strength among them. Interestingly, the HFC also shows unique pseudo-elastic behavior under large strain due to the mechanical coupling effects. The HFC is demonstrated as an elastic metal conductor, programmable sensor, and finally as an elastic mold for structure transplantation by mechanically decoupling the elastomer core from the helix fiber. The results not only deepen the fundamental understanding of HFCs, but also may promote future structure-properties and fabrication studies on helix-structured functional composite and devices.

¹ College of Polymer Science and Engineering, State Key Laboratory of Polymer Materials Engineering, Sichuan University, 610065 Chengdu, Sichuan, China.

² State Key Laboratory of Medicinal Chemical Biology, Key Laboratory of Functional Polymer Materials, College of Chemistry, Nankai University, 300071 Tianjin, China. ³These authors contributed equally: Dan Li, Zhiwei Zhu. ✉email: xuewei.fu@scu.edu.cn; liuzunfeng@nankai.edu.cn; weiyang@scu.edu.cn; yu.wang3@scu.edu.cn

Wrapping functional one-dimensional materials or devices onto an elastomer core is a well-known strategy to transforming non-stretchable/elastic materials/devices into highly stretchable/elastic helix fiber composites (HFC)^{1–3}. In spite of its wide application, fundamental studies on understanding the mechanical behaviors of the HFCs are unfortunately missing. However, with the increasing interests on flexible/stretchable functional materials/devices, the possible critical factors controlling the structures and properties of the HFCs will be essential for guiding the design and fabrication of high-performance HFCs. The elastic/stretchable behavior of the elastomer is well known by the chain conformation stretching and retraction due to entropic effects^{4,5}. On the polymer chain level, it has been recognized that the mechanical properties are fundamentally contributed by both chemical structures and chain conformation structures and behaviors^{6–9}. Similarly, in biology, the conformation structures of proteins, or more accurately, the protein tertiary structures fundamentally control their bio-functions^{10–13}. Although the significance of conformation structures has been well recognized at polymer chain level, the significance of conformation manipulation at macroscopic materials level is not well recognized. For example, for the helix fiber part of the HFC, its flexibility and stretchability are conventionally understood as deformation, not conformation changing behavior. As a result, the chain conformation changing behavior at a microscopic level and the helix deformation at macroscopic level are habitually separated and their possible connection cannot be established.

Actually, in polymer physics, the chain flexibility is defined as the ability to change its conformation structures, which may be applicable to the definition of material flexibility. Therefore, conformation structures and behaviors can be viewed as the general nature of flexible or soft materials. From this point of view, one will find that soft matter does show very similar conformation structures and behavior to polymer chains. For instance, soft ribbons are often employed as typical dance props for art performance. The ribbons are so soft that their conformation can change smoothly under the effect of gravity and

the waving force by the dancer (Fig. 1a). Similarly, the individual fiber or fiber bundle inside the ribbon also shows conformation change behavior during motion. On a molecular level, the polymer chains also undergo conformation change along with the macroscopic motion. Moreover, the wisdom of conformation motion or change possibly inspired the invention of soft metal armor, which is built through the topological interpenetration of metal loops. Even today, material technology innovation benefits a lot from conformation-based wisdom, although it has not been widely recognized. For instance, the design and fabrication of non-traditional materials via Kirigami and Origami strategies is a good example for generating conformation behaviors in materials^{14–18}. Kirigami is a traditional art of paper cutting to create arts. The cutting removes part of the paper and generates on-demand free volume that helps improve the flexibility or conformation-change capability of the resultant arts. Kirigami has recently emerged as an attractive strategy for creating shape-shifting structures^{19,20} and ultra-stretchable materials²¹. Similarly, by taking advantage of conformation-change capability of materials, Origami transforms material conformation structures from one to another simply by folding and unfolding. In fact, Kirigami and Origami have inspired numerous studies of macro-hierarchical materials with highly reconfigurable and multi-functional features^{17,22–24}.

For example, Kirigami patternization helps transform rigid and even non-stretchable materials into stretchable ones^{25,26}, and also offers a promising strategy for 2D-to-3D shape morphing²⁷. Sorrentino et al.²⁸ designed a metamaterial with enhanced mass-to-strength mechanical properties and auxetic characteristic by optimizing the geometry and connecting parts of a rotating square structure. Gosselin et al.²⁹ reported a unique transparent material with high impact absorption capability assisted by coil-conformation structured long fiber. Under impact, the imbedded coil-conformation structured filler expanded after the matrix cracked, and it changed into an extended conformation. The change of filler conformation increased the plastic deformation of the composite material and the energy dissipation capability. More interestingly, the conformation change at both microscopic

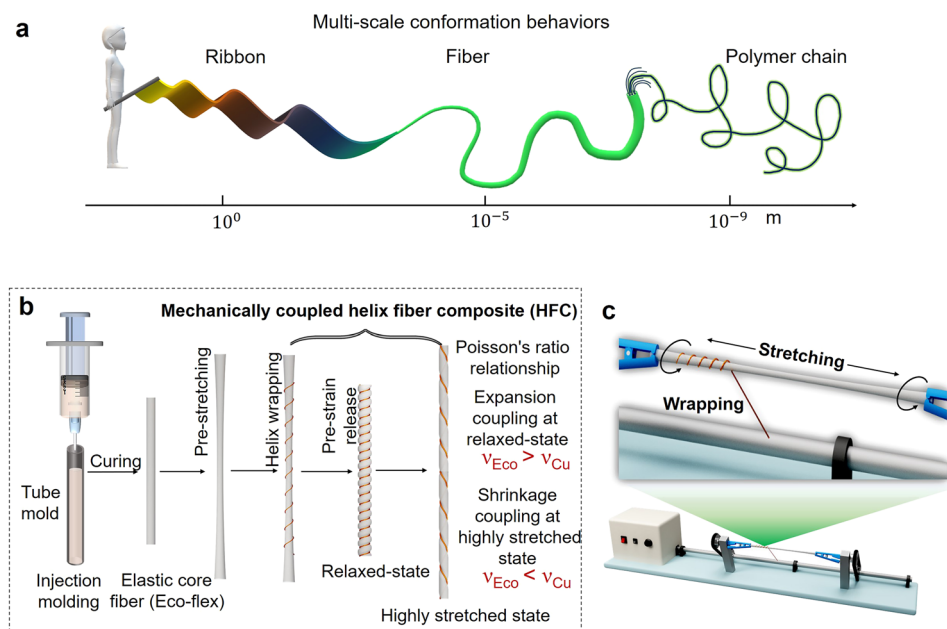


Fig. 1 Multiscale chain-conformation-like behaviors for soft matter and the design of cross-scale conformation coupled helix fiber composite (HFC). **a** The multi-scale conformation behaviors as demonstrated by a ribbon belt. **b** Schematic illustration of the typical wire-on-elastomer wrapping strategy for the preparation of helix fiber composites (HFC). ν is Poisson's ratio. **c** Schematic of the experimental setup for preparing the HFC.

and macroscopic levels for elastic fibers generated significant refrigeration effects as revealed previously³⁰. The strategy based on Origami also works for the design of flexible devices. For instance, Jiang et al.³¹ reported a type of Origami lithium-ion battery with extreme mechanical deformability, including folding, unfolding, twisting and bending.

Overall, HFC, Origami, and Kirigami inspired materials share one characteristic, they are highly flexible in shape changing due to special design of the structures. Particularly for HFCs, there is theoretically no limit for the types of elastomers and fibers for making the helix. The fiber can be either as simple as a single-component wire, or as complicated as a multi-component fiber device. At the same time, the fiber for the helix is not necessarily limited to a polymer; it can be a metal, inorganic or composite. As such, how rigid or brittle materials become flexible and stretchable materials? Based on the understanding of microscopic and macroscopic conformation, a concept of conformation materials can be defined as a type of materials with chain-conformation-like structures and behaviors at the scale beyond molecular chains. In this study, as illustrated in Fig. 1b, we propose a very facile wire-on-elastomer wrapping strategy to preparing a simple conformation material, called as helix fiber composite (HFC). This HFC is composed of two materials featured by different conformation structures. Specifically, the elastomer is featured by cross-linked random coil conformation structures on the chain level, and the wire (e.g., copper (Cu) wire) exhibits a helix conformation structure by wrapping. The helix wire is fixed by physical interlocking controlled by the pre-strain of the elastomer without adhesive. This process can be conducted via a simple wire wrapping machine as illustrated in Fig. 1c (for details, see the Experimental methods). In the following sections, we will define the geometric parameters of this HFC material and study its unique mechanical coupling behavior, mechanical properties and functions. This is possibly the first time to introduce the material conformation concept and perform a fundamental study on conformation materials via using the HFC as a model example. Reported studies with similar structures often treated them as a strategy to achieving material flexibility^{32–36} or special functions for medical care³⁷ and body armor applications³⁸. The understanding of these unique materials has barely been discussed, particularly from the perspective of conformation structures and behaviors.

Results and discussion

Fabrication of HFC. The successful fabrication of the HFC is not as simple as expected; it depends on several critical factors. In short, the key is to achieve an appropriate mechanical match between the elastomer fiber and the helix-conformation wire. To better describe the fabrication process and structures, we need to define several parameters as shown in Fig. 2a, such as the number density of helix turns on the pre-stretched elastomer per meter (T_n) and so on. At the same time, we define mechanical coupling between the helix-fiber and elastomer when the volume-exclusion interaction occurs. Figure 2b shows the relaxed structures of HFCs with different T_n . One can find that the helix conformation can generate different states with the elastomer core fiber. If T_n is less than a critical value (T_c), the helix conformation will detach from the elastomer at the relaxed state, which is defined as decoupled state. In this case, the diameter of the helix-coil (D_r) is larger than the diameter of the elastomer fiber (D_0). If T_n reaches the critical value of T_c , the helix conformation will start to interact with the elastomer fiber and D_r will be equal to D_0 . This indicates the initially coupled state. Further increase of T_n will finally generate strong coupling state between the helix conformation and elastomer fiber, and D_r will

be less than D_0 . It is noted that the length at relaxed state (L_r) will be larger than the initial length of the elastomer due to the helix-conformation coupling effects. At coupled state, the relationship between the HFC spiral spacing and the diameter of the coil can be described by a simple triangular geometry, as shown in Fig. 2c. At the relaxed state, the total contour length of helix conformation (L_h) remains unchanged, and the total number of wrapping turns, n , also does not change after the relaxation of pre-stretching. The geometry relationship among the parameters is summarized by the following Eqs. (1) and (2):

$$P = L/n \quad (1)$$

$$D_r = \frac{\sqrt{L^2 - \left(\frac{L}{n}\right)^2}}{\pi} = \frac{\sqrt{L_h^2 - L^2}}{\pi n} \quad (2)$$

At the initially coupled state, $D_r = D_0$ and $L = L_0$. Therefore, the critical total turn number n_c and T_c can be calculated by Eqs. (3) and (4):

$$n_c = \frac{\sqrt{L_h^2 - L_0^2}}{\pi D_0} \quad (3)$$

$$T_c = \frac{n_c}{L_s} = \frac{\sqrt{L_h^2 - L_0^2}}{\pi D_0 L_s} \quad (4)$$

Based on Eq. (4), the value of T_c is calculated to be 149. This value is consistent with the experimental result which is around 145, as shown in Fig. 2d. The above three states of the elastomer/wire composite can be clearly observed in Fig. 2d. Here, it should be noted that the HFC is successfully prepared only when the elastomer/wire composite is at coupled state. By measuring the length of the HFC at relaxed state (L_r), one can distinguish the different states in Fig. 2e. Due to the coupling effects, L_r will not return to its original length of the elastomer fiber. Therefore, the degree of coupling strength (D_{cs}) can be determined by Eq. (5):

$$D_{cs} = \frac{\Delta L}{L_0} = \frac{L_r - L_0}{L_0} \quad (5)$$

Another interesting phenomenon is that the diameter of Cu wire (d_f) plays a critical role in the successful fabrication of high-quality HFCs. As shown in Fig. 2f, when the diameter of the Cu wire increases to above 100 μm , the composite shows uncontrollable lateral deformation and cannot return to its original straight configuration, which can be understood as uncontrolled conformation-change behavior during relaxing. It is believed that this behavior is fundamentally related to the mechanics of the Cu helix-conformation structure, which can be simply defined as conformation mechanics. The possible mechanism for the uncontrollable conformation-change behavior is illustrated in Fig. 2g. It shows the force and deformation evolution during relaxing for both the elastomer core and the coupled Cu helix-conformation wire. Theoretically, the resistance force (F_s) of the Cu-helix spring should be in line with the retractive force (F_e) of the elastomer if the HFC composite is strictly straight during the relaxing process. In this case, no transverse force (F_f) will be generated. However, in practice, it is likely that they are not perfectly in line with each other due to the softness of the components and non-uniform geometry of the structures. Under this situation, transverse force will be generated at some locations. It should be noted that the existence of transverse force not necessarily leads to transverse deformation, which occurs only when the transverse force is greater than a critical bending yielding force (F_t) of the HFC composite. This critical yielding force should be related to the bending modulus of both the elastomer and the Cu helix conformation. It is expected that, the

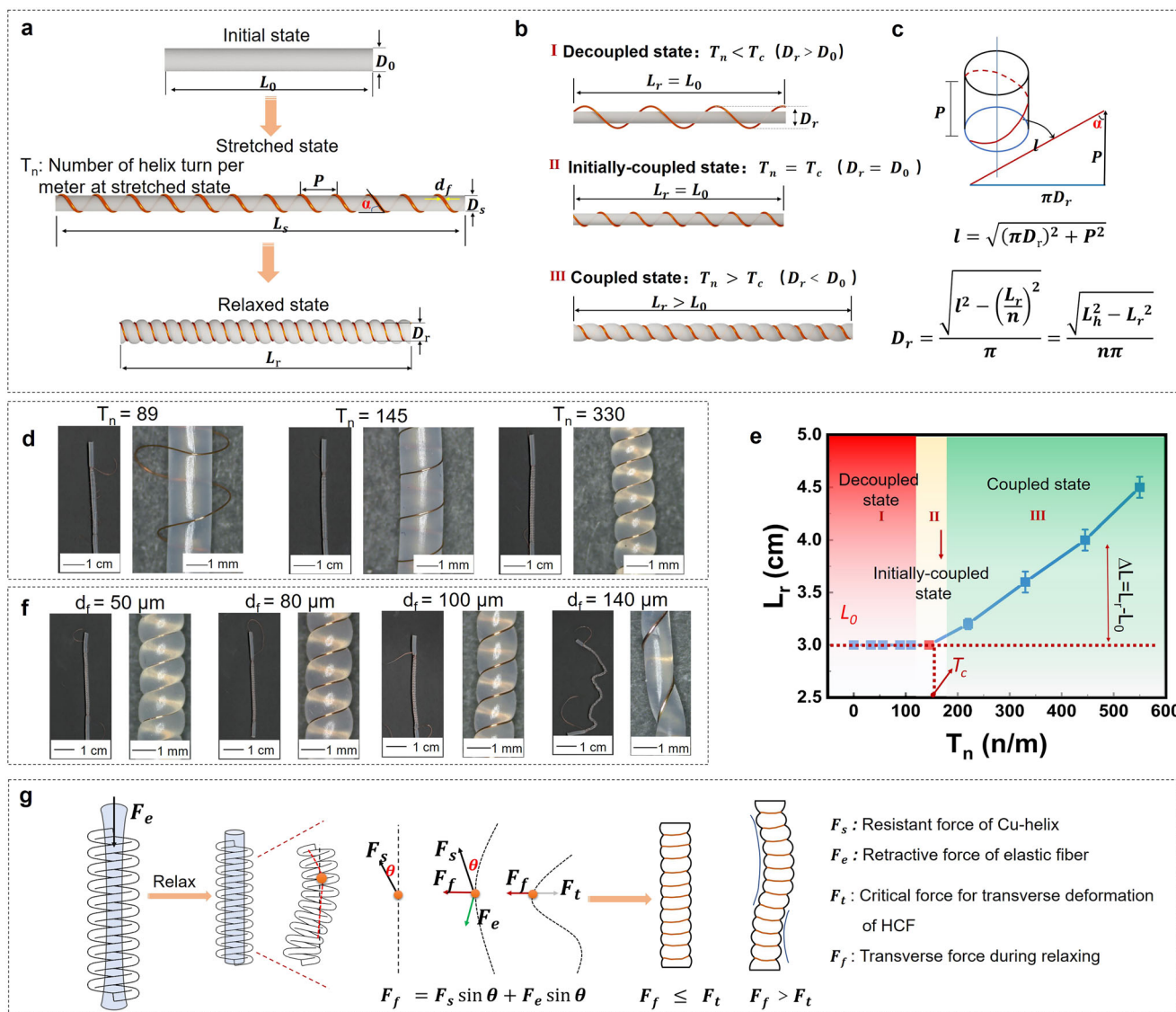
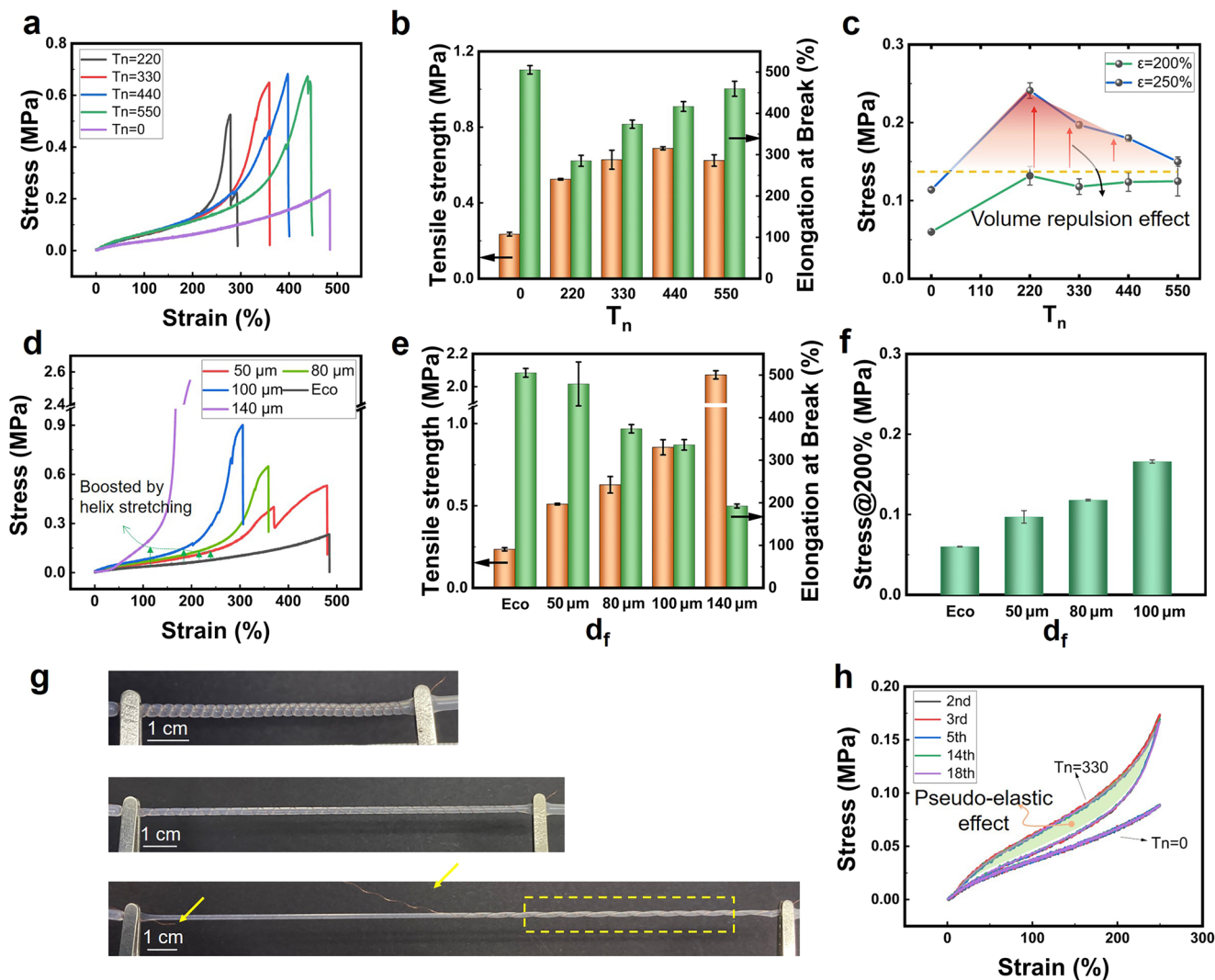


Fig. 2 Fabrication studies and structure analysis of the HFC. **a** Definition of the controlled parameters for the fabrication of the HFC. **b** Schematic diagram of the different states for the Cu wire-wrapped-elastomer composites, including the decoupled, initially coupled and strongly coupled states. A high-quality HFC is successfully fabricated only when the two components are mechanically coupled. **c** Illustration of the trigonometric relationship for the Cu helix-conformation structures at coupled states. **d** Photographs of wire-wrapped-elastomer composites with different T_n values corresponding to different coupling states from decoupled, initially coupled and strongly coupled states. **e** The dependent behavior of the length of the wire-wrapped-elastomer at relaxed state, L_r , on the T_n value, which can distinguish the different states as introduced above. **f** Photographs of HFCs prepared by wrapping Cu wires with different diameters. **g** Force analysis for understanding the uncontrollable bending behavior of HFC with thick Cu wire.

larger the diameter of the Cu wire, the higher the bending/compression modulus and thereof the resistance force of the helix (F_s). Since the transverse force comes from the resistance force, a thick helix conformation can lead to a higher transverse force than the critical transverse yielding force of the HFC composite. However, if the diameter of the wire is too high to be bendable, the transverse force may not be able to conquer the critical bend yielding force of the helix, which is beyond the scope of this study. In short, the successful fabrication of high-quality HFCs requires the control of several critical parameters, such as the turn number density (T_n) and the diameter of the wrapping wire (d_f). The mechanics of the helix conformation may play a critical role in the fabrication.

Programmable and pseudo-elastic mechanical behavior of HFC. The mechanical properties of the HFC were investigated by

tensile testing. Figure 3a shows the stress–strain curves for the HFC with different T_n . One can find that the stress–strain curves of the HFCs are obviously different from the pure elastomer of Ecoflex. Specifically, the HFCs show higher modulus and ultimate tensile strength than the pure elastomer. As the T_n increases, the ultimate tensile strength increases and the elongation at break also increases as shown in Fig. 3b. This result is worthy of discussion for the following reasons. First, the coupling effects between the macro-helix conformation structure and the microscopic chain conformation can notably improve the mechanical properties of the HFC composite. Second, one can expect a synergistic effect from the conformation coupling behaviors since the mechanical strength and elongation strain at break are simultaneously improved with the increase of T_n . This synergistic effect is very difficult to achieve for conventional materials as a high mechanical strength is usually contradictory to a high strain at break. For the Cu helix, the elongation at break increases 20



times with the increase of helix number (Supplementary Fig. 1), which is essentially contributed by the stretching of the helix conformation. Figure 3c shows the tensile stress of the HFCs with different T_n with pre-stretched strain of 200% or 250%. Particularly, at the pre-stretched strain of 200%, the stress of the HFCs is independent on T_n , while it is still higher than the pure elastomer. When the strain is above the strain of pre-stretching for wrapping, for example, at the strain of 250%, the stress of HFCs decreases with the increase of T_n . This result is somehow counterintuitive as the stress is expected to increase with the increasing of coupling strength or T_n . This unusual behavior may indicate some additional coupling effects between the helix and elastomer, which should be related to the volume repulsion effect during the conformation stretching of the copper helix. The volume repulsion effect happens when the expanded helix conformation is stretched into a shrunken helix conformation with a diameter less than that of the stretched elastomer. This effect usually happens when the stretched strain is above the pre-stretched strain (200%), and its strength weakens with the increasing of T_n as

shown in Fig. 3c. The structural changes of the HFC composite during tensile process are shown in Supplementary Fig. 2. One can observe that the volume repulsion interaction between the helix conformation and the elastomer causes an obvious compression effect on the elastomer. When the helix and elastomer are close to be fully stretched, the macroscopic helix conformation and the microscopic chain conformation take straight line like conformation^{34,39}, which is usually very difficult to achieve in practice.

In addition to the torsion number density, T_n , the diameter of the Cu wire is found another critical parameter affecting the mechanical properties of the HFCs. As shown in Fig. 3d, e, with the same T_n of 330, the larger the diameter of the Cu wire, the greater the ultimate tensile strength of the HFC. At the same time, one can observe notable mechanical contribution of the macro-helix conformation stretching as indicated by the arrows in Fig. 3d. The stretching of macro-helix conformation becomes harder with the increasing diameter of the wire. However, the elongation at break of HFC is reduced with the increasing of wire

diameter. As the diameter of Cu wire increases, the interaction area between the helix conformation and elastomer also increases. Therefore, the volume repulsion effects and tensile strength will be enhanced. The decrease of elongation strain with the increase of wire diameter indicates that the volume repulsion effect can accelerate the break of elastomer (see Fig. 3e). The volume repulsion effect can also be observed even at the strain 200% (the pre-stretched strain for wire wrapping) as shown in Fig. 3f, which may result from the contact force during wrapping. The breaking behavior of the HFCs is also worthy of discussion. Depending on the cases, the breaking occurs for either the elastomer or the helix wire. Interestingly, no matter which component fails first, the helix-elastomer conformation coupling does not disappear with the failure. As shown in Fig. 3g, during the entire stretching process, the Cu wire is not separated from the elastomer directly after its breaking. The surface morphology of failed HFC is shown in Supplementary Fig. 3. It can be seen that the surface of the failed HFC has obvious concave indentation, which is more obvious for the sample wrapped by thicker Cu wires. This finding indicates that there is a strong interaction between the Cu wire and the elastomer. This morphology should be the direct proof of the volume repulsion effects, as discussed previously.

Another interesting behavior for the HFCs is the mechanical hysteresis phenomenon as shown in Fig. 3h. It should be noted that the hysteresis phenomenon is well known in magnetic materials, but not very common in polymer composites. For example, the elastomer without the coupling effects from the helix conformation does not show this behavior during the load-unload cycling test. In contrast, the HFC composite with T_n of 330 shows obvious hysteresis loop phenomenon. This result indicates that the deformation of the HFC composite is composed of non-elastic component as explained below. Different from the chain conformation with remarkable entropy elasticity, the entropy change of the Cu helix conformation during stretching will not lead to detectable entropy elasticity. It should be noted that the helix-conformation structure does show elastic behavior in a very limited range of strain since it can be viewed as a soft spring. As a result, a large strain (e.g., above 100%) for the helix conformation will include a large portion of plastic deformation. This plastic deformation will finally be retracted by the elastic force of the elastomer during unloading due to the strong coupling effects, which gives rise to a pseudo-elastic behavior for the Cu helix conformation. The concept of pseudoplastic fluids is well known for polymeric melts or solutions; however, pseudo-elastic behavior has rarely discussed for traditional materials. Therefore, the unique mechanical properties of the HFCs, as shown above may inspire the design of conformation materials with special properties/functions.

Simulation studies of the mechanical coupling of HFC. To better understand the mechanical properties of the HFCs, we divide the stress-strain curves of the samples into three regions based on the understanding of the conformation stretching process for both elastomer and the macroscopic helix conformation. For comparison, Fig. 4a shows the chain conformation change of the pure elastomer during stretching. Basically, the three different regions of the stress-strain curve for pure elastomer are the coil-state region (I) at the beginning of the stretching, the medium-stretched region of partially-stretched chains (II), and strong stretched region of oriented chains (III)^{38,40,41}. In the coil-state region, the chain conformation varies around its equilibrium configuration and shows Hooke elastic behavior⁴². In the coil-to-stretch region, the chain conformation undergoes a change with little increase in stress. As the stretching reaches the third region of stretched orientation, the chain conformation is strongly

stretched into orientation configuration, and stress climbs rapidly with the strain until the final failure of the elastomer.

For the HFCs, the cross-scale conformation change at both microscopic chain level and macroscopic helix level is illustrated in Fig. 4b. Similarly, there are also three different regions as introduced for pure elastomer. However, the strong coupling due to the volume repulsion effects between the two components significantly change the conformation behavior as discussed below. We note that the coupling state is determined by both the volume expansion and repulsion in different conformation change state. In the first region of expansion coupling state (strain up to 100%, also known as linear elasticity region), Poisson's ratio (ν) of the elastomer (0.42 ± 0.06) in the linear elasticity region is larger than that of the Cu helix (0.31 ± 0.03) with a T_n of 220 and d_f of 50 μm , for instance (see Supplementary Tables 1, 2 for the detailed data). In this state, the helix-conformation can feel the volume expansion force of the elastomer, and in turn, the chains in the coupling area can feel the compression force from the helix conformation. Therefore, the chain conformation will take a different shape depending on its location. For the part without the coupling effects from the macro-helix, the chain will go back to its relaxed coil-conformation after releasing the pre-stretched strain. However, for the coupling part, the chain will form stretched conformation due to the volume repulsion effects, which has been described by the coupling strength (see Eq. (5)). The chains with stretched conformation can be viewed as self-reinforcement component, which leads to improved modulus for the elastomer. In the second region (strain up to 250%), the expansion-to-weak coupling transition occurs. Both the helix conformation and chain conformation experience stretching, and the coupling force between the helix conformation and the elastomer reduces with stretching. However, Poisson's ratio of the elastomer decreases to 0.17 ± 0.03 , which is smaller than that of the Cu helix. Therefore, the elastomer starts to suffer from the shrinkage of the Cu helix. As the stretching continues, the HFCs undergoes a state of shrinkage coupling, when Poisson's ratio of the elastomer decreases to 0.08 ± 0.01 , smaller than that of the Cu helix. In this state, the diameter shrinkage of the helix is faster than that of elastomer, which will generate coupling/contact force again due to the volume repulsion effect. In this region, the stretched helix conformation creates compression effects onto the oriented chains, leading to fast stress growth as illustrated by Fig. 4b.

It was also found that the pre-stretched strain has little effect on the mechanical properties of the HFCs (Supplementary Fig. 4). The stress-strain curves of the HFCs prepared by 100%, 200% and 300% pre-stretched strain nearly coincide with each other, which was also observed for the HFC composite with large size of wire diameter. The above behavior seems counterintuitive as it is believed that a higher pre-stretched strain could lead to stronger coupling effects, and thereof higher modulus. However, if one takes a close look into the stress growth curve in the range from 100% to 300% for the pure elastomer, the stress is less dependent on the strain in this range. In other words, the pre-stretched strain in this range does not notably change the coupling strength. In fact, most the above results indicate that the torsional number density, T_n , is a critical parameter controlling the coupling strength and so the mechanical properties of the HFCs. Based on this finding, it will be attractive to regulate the mechanical properties of HFCs simply by controlling the T_n of the macroscopic helix conformation, as illustrated in Fig. 4c. Theoretically, if we can establish the relationship between the T_n and the mechanical properties, it is totally possible to precisely tune the mechanical properties of the HFC composite by controlling the structural parameter of the helix conformation, T_n .

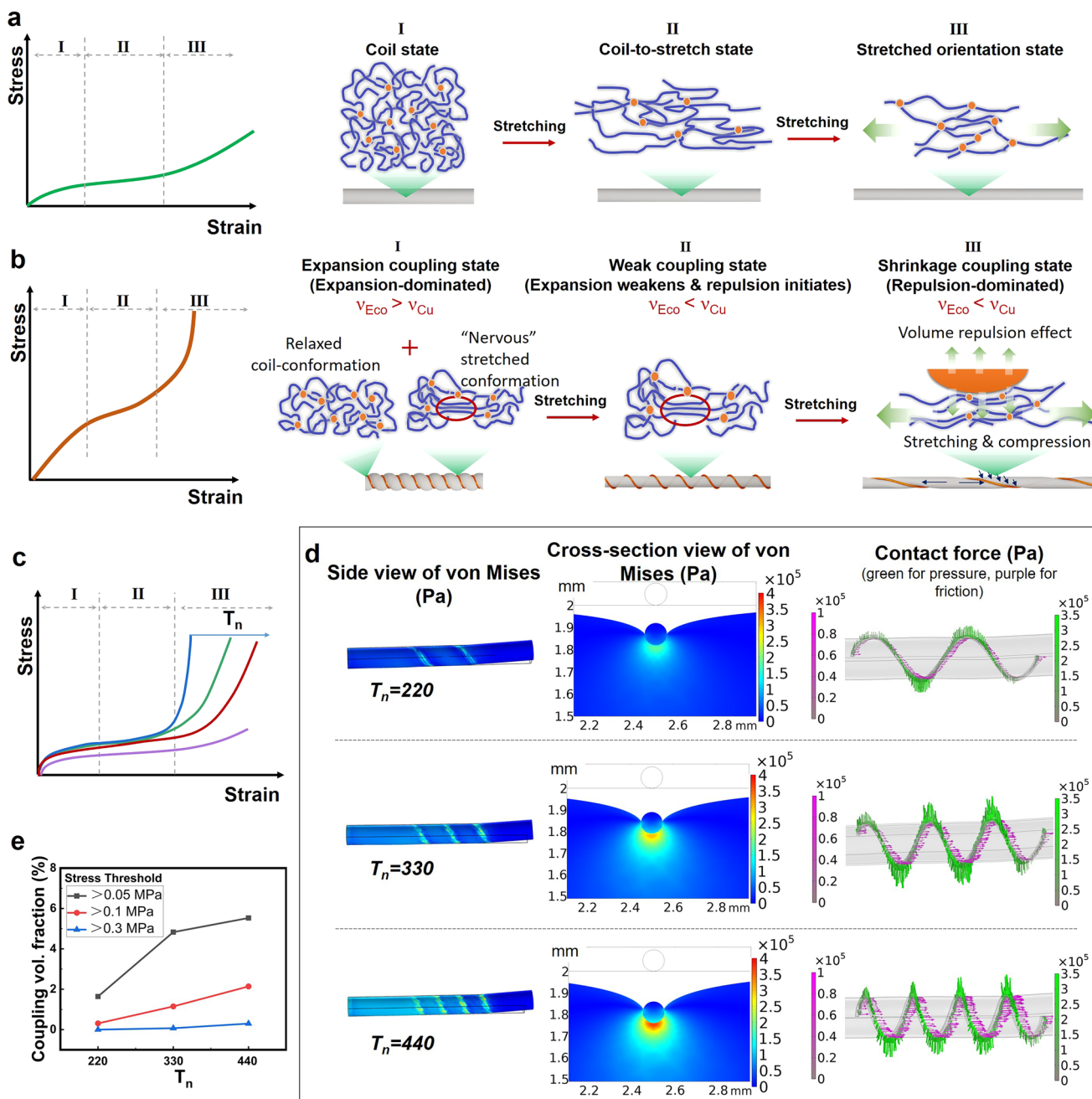


Fig. 4 A conformation coupling mechanism for understanding the mechanical properties of the HFCs. **a** Schematic of elastomer chain conformation changes during stretching without the coupling effects from the wire macro-helix conformation. **b** Schematic of the elastomer chain conformation changes for the HFC with strong coupling effects from the macro-helix conformation. ν is Poisson's ratio. **c** Illustration of tuning the stress-strain curves of HFC by torsion number, T_n . **d** Simulation study of the mechanical coupling for the HFC with different T_n based on finite element analysis by COMSOL Multiphysics. The coupling effects can be described by the von Mises distribution caused by the compression of the helix conformation. **e** The dependent behavior of coupling volume fraction inside the elastomer on the torsion number, T_n .

To demonstrate this great potential, the coupling effects were further studied by finite element analysis by using COMSOL Multiphysics, and the results are shown in Fig. 4d. Here, to simulate the conformation coupling, the elastomer is pre-stretched with a strain of 200% as employed in experiments. Then, the Cu helix conformation with the same diameter to the stretched elastomer is co-axially put onto the stretched elastomer. By releasing the strain, the helix conformation is successfully coupled with the elastomer due to the diameter expansion of elastomer. It is noted that the above simulation was performed with one end of the elastomer fixed, in order to achieve good

convergence for the simulation (for details, see the Experiment methods). Assisted by the simulation studies, the side view and cross-section view of the von Mises stress and the contact stress have been calculated in Fig. 4d. One can find that, the coupled area and the von Mises stress inside the coupled area of elastomer both grow with the increasing of T_n (also see Supplementary Fig. 5 and Supplementary Table 3). Meanwhile, the contact stress and friction force at the interface also depends on T_n in the same way. These simulation studies not only confirm the strong coupling effects from the helix conformation but also establish the relationship between the coupling effects with the torsional

number density T_n . For example, if we define a threshold value for the von Mises stress to determine the coupling effects, then the coupling volume fraction inside the whole elastomer can be calculated by integral operation along with the helix conformation as shown in Fig. 4e. One can find that the coupling volume fraction basically linearly depends on T_n , which makes it possible to precisely tune the mechanical properties of the HFCs. In short, the conformation coupling effects with volume repulsion interaction between the cross-scale conformational components play a leading role in the mechanical properties of the HFCs. It should also be noted that the above coupling behavior is not unique to Cu wire, while other fibers or wires can work in a similar way (Supplementary Fig. 6). This universal behavior indicates a general solution for the fabrication of various types of chain-conformation-like materials.

HFC for functional materials and structure transplantation.

The HFC combines the advantages of elasticity from the elastomer core and electrical conductivity from the helix-conformation metal fiber, imparting a unique function being as a highly stretchable and durable conductor. As shown in Supplementary Fig. 7a, the resistance of the HFC is nearly unchanged during the stretching-releasing testing with varying strains from 50% to 250%. With a fixed strain of 100%, the resistance stays about 0.83 Ω during the repeated stretching-releasing testing for about 1900 cycles as shown in Supplementary Fig. 7b. It is interestingly found that the HFC shows much better durability than the Cu wire upon cyclic bending with 180°. As shown in Supplementary Fig. 7c, after about 3500 bending cycles the HFC remains a low resistance of 0.76 Ω . While, for the pristine straight-line Cu wire without helix-conformation structures, it breaks after 58 bending cycles due to the metal fatigue (see the inset in Supplementary Fig. 7c). The above flexibility of stretchable conductor should be understood as the benefits of the cross-scale teamwork of conformation structures. Specifically, the coupled structure evolution of elastomer chain conformation and Cu helix conformation generates good elasticity and anti-fatigue capability for the HFCs. The large strain of stretching or bending for the Cu helix is realized by its conformation structure change, not by the bulk stretching or bending of the metal wire. Therefore, the conductivity of the helix conformation is very stable during the deformation. This flexibility enabled by conformation change will be very attractive for the design and fabrication of practical functional materials and devices.

To further demonstrate its potential for the design and fabrication of non-traditional functional materials, we prepared a type of biomimetic HFC sensor based on conductive thermoplastic polyurethane (TPU) nanocomposite fiber. The conductive TPU nanocomposite fiber was composited with 20 wt % carbon nanofillers (i.e., carbon black and carbon nanofiber with a mass ratio of 3: 1), and the fiber surface was coated with silver to increase the sensitivity and conductivity. The diameter of the sensor fiber was about 550 μm . Similar to the above stretchable conductor, the conductive TPU sensor fiber was wrapped onto the elastomer with a helix conformation. Conventionally, fiber sensors with a straight-line conformation will respond to the strain/stress very quickly as illustrated in Fig. 5a and Supplementary Fig. 8. In other words, the required strain to activate the sensing properties (that is, activation strain) is very small. Interestingly, for the smart HFC sensor, it possesses a high activation strain compared to the conventional sensor as shown in Fig. 5a. Benefitting from the helix-conformation structure, the sensing property will be activated when the strain is above the activation strain, which should correspond to the starting point for the bulk stretching (not the conformation stretching) of the helix sensor fiber. To better understand this point, one can divide the process into three stages. For stage I, it is actually a helix-

conformation stretching region, meaning that strain is dominated by the helix-conformation stretching not the bulk fiber itself. This process is akin to the conformation stretching of wrinkle skin at the finger joint. As the stretching continues, the intensity of conformation change weakens, and there is a transition from conformation-dominated to bulk-dominated stretching, namely, stage II. This is analogous to the flattened skin without the wrinkle conformation structure when we bend our finger to a certain degree. At this point, we can feel the tension of the skin and the sensor can tell the bulk stretch of the sensor fiber. For stage III, the bulk stretching of the sensor fiber dominates the process. In this region, the resistance of the sensor fiber is strongly affected by the growth of stretching strain.

The curves of $\Delta R/R_0$ versus strain for the HFC sensors with various torsion number density (T_n) are shown in Fig. 5b. One can find that the activation strain increases notably with the increasing of T_n . Specifically, when increasing T_n to 200 or 400, the activation strain raises up to 125% or 175%, respectively. This activation strain phenomenon was also reported by Fink et al.⁴³ recently. In their study, they report another two interesting strategies for fabrication of helix metal wire filled composites by harnessing the buckling instability in a metal micro-wire within a thermally drawn elastomer fiber, and by twisting an elastomer fiber to yield helix wire embedded in elastomer. Compared with other strategies, the sensor by HFC-based strategy as shown in this study can achieve much higher activation strain. At the same time, one can establish the relationship between the activation strain and T_n as shown in Supplementary Fig. 9. With this relationship, the activation strain is also programmable by precisely controlling T_n of the HFC sensors. Although high sensitivity is usually desired, non-traditional sensors^{44–46}, as shown by the HFC sensor with programmable activation strain may find significant applications in biomedical engineering, aerospace engineering and so on.

Furthermore, the mechanically coupled HFC can also be employed as a unique template for structure transplantation. The process of structure transplantation via the HFC template is illustrated in Fig. 5c. First, the HFC template is put into a tube mold and then filled with epoxy resin. After curing, the elastomer part of the HFC is mechanically decoupled from the helix wire and the cured epoxy. Depending on whether the helix-wire is fixed inside the cured epoxy, we can prepare two types of structure-transplanted products, including epoxy tubes with helix-channel only and epoxy tubes with both helix-channel and helix-wire. Theoretically, one can flexibly design the helix microstructures of the epoxy tubes by precisely controlling the initial helix structures of the HFC. The prepared structure-transplanted products with different helix structures are shown in Fig. 5d and e (more by Supplementary Fig. 10). One can find that the helix structures of the HFC are completely replicated and successfully transplanted. This fabrication by HFC transplantation may open the potentials for the fabrication of functional composites. Additionally, the HFC can be functionalized by optical fiber as shown in Supplementary Fig. 11. By wrapping the luminescent fiber onto the elastomeric fiber, one can prepare a type of helix-light-conformation composite which can generate elastic-like conformation of light during the stretching and releasing of the elastomer. This may be used for light-based art performance. In short, the above studies are only a few examples, and the broadened potential of conformation materials as exemplified by the helix-fiber composites (HFCs) is waiting for exploration.

Conclusion

In summary, we have demonstrated the fabrication, mechanical coupling behaviors, unique mechanical properties and

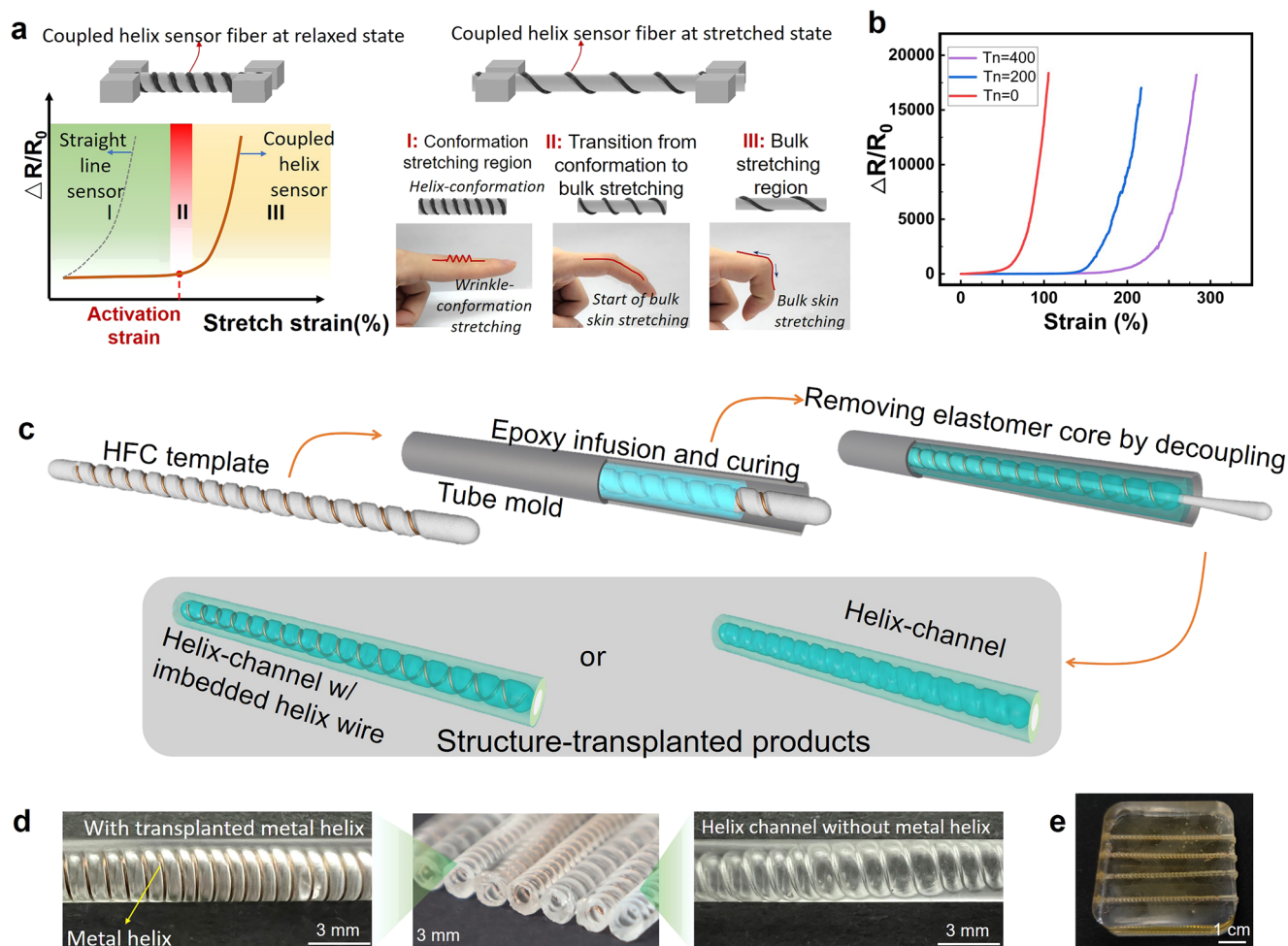


Fig. 5 Demonstration of HFC as an innovation platform for the design and fabrication of helix-structured functional composites. **a** Illustration of HFC-based biomimetic smart sensor with helix-conformation structure for realizing programmable activation strain for unique sensing application. The conformation change behavior of finger skin during finger motion is also demonstrated to help the understanding of the helix-conformation change of the sensor fiber mechanically coupled with the elastomer core. **b** The unique strain sensor properties of HFC and the regulation of the activation strain for the HFC sensor materials by the torsion number, T_n , respectively. **c** Illustration of the concept of structure-transplantation by stretching-based mechanical decoupling operation of the HFC. **d** Photographs for the structure-transplanted tube products from the HFC, with or without the transplanted metal helix. **e** Photograph of an epoxy cuboid with metal-helix array structure by HFC-based structure transplantation.

applications of a type of helix fiber composites (HFCs). Specifically, for the successful fabrication of HFCs, two factors have been found critical, including the mechanical match and appropriate mechanical coupling between the elastomer core and the macroscopic helix-wire, which can also be understood as a cross-scale conformation coupling. The mechanical coupling has been realized simply by volume exclusion effects, which depends more on the torsional number density T_n of the helix conformation compared to the pre-stretched strain of the elastomer. For the mechanical properties, the T_n and mechanical properties of the helix-wire or helix conformation are found keys to control the coupling effects inside the HFCs and thereby the mechanical properties. Interestingly, one can achieve not only programmable mechanical properties for the HFCs by precisely tuning the T_n value, but also unique mechanical hysteresis property due to a non-conventional pseudo-elastic behavior. Finally, for the functions, the HFC provides a promising solution to the design and fabrication of elastic metal conductor, programmable sensor materials and elastic mold for structure transplantation. In short, this study may open an avenue for composite innovation by learning from the microscopic chain-like conformation structures and behaviors.

Methods

Materials. Monofilament copper (Cu) wires (Cu \geq 99.99%) with different diameter of 50, 80, 100, and 140 μm were purchased from Wanda Metal Co., Ltd. (Hebei, China). Silicon rubber (Ecoflex 00-30) was purchased from Smooth-On, Inc. Thermoplastic polyurethane (TPU, Elastollan 1185A FHF) was purchased from BASF, Co., Ltd. carbon black (Super C65) and carbon nanofiber were purchased from Guangdong Canrd Energy Technology Co., Ltd. Conductive silver paint and polyamide (PA) fiber were purchased from Alibaba.

Preparation of HFC. First, the silicon rubber precursor solution was prepared by mixing the component A and B in a 1:1 weight ratio for 3 min until homogeneity. The bubbles were removed by pumping air in a vacuum oven for 4–5 min. Second, the above solution was injected into a polyethylene tube with inside diameter of 2 mm through a syringe by injection molding. After curing at room temperature for 4 h to form an elastomer core. Third, the elastomer core was pre-stretched at a strain of 200%, and then a Cu wire, PA fiber, or UHMWPE fiber was wrapped around the elastomer core using a semi-automatic winding device (Fig. 1c). In this process, the stress, wrapping angle, and the rotation speed of the elastomer fiber were carefully controlled to vary the number of turns (or T_n , number of turns per meter at stretched state) and the distance between adjacent spirals.

Preparation of TPU-based conductive fiber. TPU-based conductive fibers were fabricated by wet-spinning. First, 0.5 g of the conductive fillers containing carbon black and carbon nanofiber (3:1 by mass) were dispersed in 10 mL Dimethylformamide (DMF) solvent, followed by sonicating for 20 min by using an Ultrasonic Homogenizer (SCIENITZ-IID, China) to obtain a uniform dispersion. Then,

2 g of TPU was added to the above mixture under stirring for 6 h at room temperature to obtain the spinning solution. Then, the mixture was transferred to a 5 mL syringe with a 20 G needle. The spinning solution was extruded into the deionized water coagulation bath for 30 min to completely solidify and then dried in the air at room temperature. Then, the as-prepared conductive fiber was sprayed by using the silver paint and then wrapped onto the Eco-flex fiber in a helix conformation by using the same procedures introduced above. The generated HFC was then used for the sensing study.

Characterizations and measurements. The morphology of all the samples was characterized by digital microscope (AOSVI, China) and digital camera. All the stress-strain curves were achieved by stretching the samples at room temperature via a universal testing machine (INSTRON, USA). The HFC was clamped to ensure both Cu wire and elastomer fiber were firmly fixed. For the measurement of tensile properties, the tensile rate was fixed at 100 mm min⁻¹ and the sample length was kept constant as 3 cm. For the loading-unloading testing, the strain was fixed to be 250% with a stretching speed of 100 mm min⁻¹. All the mechanical measurements were repeated at least 5 times for data reliability. For Poisson's ratios testing, the sample size under different strains was determined through image acquisition, and then, Poisson's ratio of the sample was determined by Eq. (6):

$$\nu_{xy} = -\frac{\epsilon_x}{\epsilon_y} \tag{6}$$

where ν_{xy} is Poisson's ratio, ϵ_x is the true transverse strain, and ϵ_y is the true longitudinal strain. Image analysis and strain measurements for these samples were carried out based on previous work by Sloan et al.³⁶ A high magnification, non-contact video system was used to accurately record the longitudinal and lateral size of the samples under different strain. A digital camera acquired the images through a variable zoom lens mounted at a fixed working distance of approximately 80 mm from the sample. The field of view was selected at the start of testing and remained fixed throughout the test. The measurement was repeated for three times for each sample in order to get more reliable data. Then the sample dimensions were measured by the tool in the PS software.

The resistance of the samples was measured by digital multimeter under cyclic 180° bending-releasing testing. The tensile fatigue performance of the samples was performed at a rate of 1 Hz with a constant strain of 100% by using a tensile machine (BOSE, USA) coupled with a digital multimeter to record the resistance data synchronously. The sensing performance was measured by resistivity measurement system (Keithley, 2400 source meter, USA) coupled with a homemade stretching equipment with a tensile rate of 0.2 mm s⁻¹.

Simulation. The commercial finite element software package COMSOL Multiphysics was used to couple the equation of motion for solid mechanics given by Newton's second law, and the stress-strain behavior of the Ecoflex restricted by the copper wire was theoretically studied. The hyper-elastic material models and linear elastic material were applied to the Ecoflex and copper, respectively. During calculation, the constitutive model of eco-flex was the two-parameter Mooney-Rivlin model⁴⁷ with C_{10} of 0.1 MPa and C_{01} of 0.05 MPa. The compression depth of helix-fiber was determined by image analysis as used for the calculation of Poisson's ratios. The values of 0.18, 0.21 and 0.24 mm were determined for the samples with T_n of 200, 300, 400, which were used as input variables for the 3D FEM model for subsequent calculation. In 3D model, we divided the calculation process into three parts. Firstly, prestretching of Ecoflex under steady state. Then, the copper wire was moved toward the restricted area. Finally, the Ecoflex retracted under the copper wire using transient calculation. In order to acquire the better convergence of the calculation model, we fixed one ending face of the Ecoflex. With the help of 3D model, we specifically study the stress and deformation of elastomer. In 2D model, we studied stress distribution when the cross-section was compressed to a certain depth. According to the relationship of C_{10} , C_{01} and shear modulus μ , which were described as $\mu = 2(C_{10} + C_{01})$, we also calculated the stress of Ecoflex section to analyze the measure of the limited area inside the Ecoflex. The detailed process are as follows.

To address the problems of deformation and stress analysis of solid materials, it is a common way to use the equation of motion based on Newton's second law. We applied such equation in the form of the second Piola-Kirchhoff stress tensor into FEM model of 2D and 3D. The general form is shown by Eq. (7):

$$\rho \frac{\partial^2 \mathbf{u}}{\partial t^2} = \nabla \cdot (\mathbf{FS})^T + \mathbf{F}_V \tag{7}$$

where \mathbf{S} is the second Piola-Kirchhoff stress tensor; \mathbf{F} is the strain gradient tensor; \mathbf{u} is the displacement term; ρ is the mass density of material; \mathbf{F}_V is the volumetric force tensor. With appropriate initial and boundary conditions, we can obtain the von Mises stress of elastomer after solving this transient partial differential equation.

More details, variables in the equation can be related to other deformation tensors to show the calculation process by Eq. (8):

$$\begin{cases} \rho \frac{\partial^2 \mathbf{u}}{\partial t^2} = \nabla \cdot (\mathbf{FS})^T + \mathbf{F}_V \\ \mathbf{S} = -p_w J_{el} \mathbf{C}^{-1} + 2 \frac{\partial \mathbf{W}_{iso}}{\partial \mathbf{C}} \\ J_{el} = \det(\mathbf{F}) \\ \mathbf{F} = \mathbf{I} + \nabla \mathbf{u} \end{cases} \tag{8}$$

Where, \mathbf{C} is right Cauchy-Green deformation tensors; p_w is the auxiliary stress; J_{el} is volume ratio; \mathbf{I} is the isochoric invariants; \mathbf{W}_{iso} is the isochoric strain energy density of elastomer. In Eq. (8), we can note that the second Piola-Kirchhoff stress is related to the energy density function and deformation variables which can help us apply the material model for the next step. Also, with the help of these tensors, we can easily apply the stress-strain parameters of solid materials to the equation. For example, the Cauchy stress ($\boldsymbol{\sigma}$) and strain values ($\boldsymbol{\epsilon}$) which we are familiar with can be calculated in the model according to Eq. (9):

$$\begin{cases} \boldsymbol{\sigma} = \mathbf{J}^{-1} \mathbf{F} \mathbf{S} \mathbf{F}^T \\ \boldsymbol{\epsilon} = \frac{1}{2} (\mathbf{F}^T \mathbf{F} - \mathbf{I}) \end{cases} \tag{9}$$

For a hyper-elastic material, its strain energy density can be expressed according to Eq. (10):

$$\mathbf{W}_s = \mathbf{W}_{iso} + \mathbf{W}_{vol} \tag{10}$$

where \mathbf{W}_s is the strain energy density of Ecoflex; \mathbf{W}_{vol} is the volumetric strain energy density of Ecoflex. The volumetric strain energy density, \mathbf{W}_{vol} , was defined as an expression of the elastic volumetric deformation (J_{el}). The quadratic volumetric strain energy density was defined as Eq. (11):

$$\mathbf{W}_{vol}(J_{el}) = \frac{1}{D_1} \kappa (J_{el} - 1)^2 \tag{11}$$

We used the two-parameter Mooney-Rivlin model to simulate the stress-strain behavior of the Ecoflex. In constitutive equation of the model, the isochoric strain energy density was written in terms of the two isochoric invariants of the elastic right Cauchy-Green deformation tensors⁴⁷. The expression can be shown by Eq. (12):

$$\begin{cases} \mathbf{W}_{iso} = C_{10} (\mathbf{I}_1 - 3) + C_{01} (\mathbf{I}_2 - 3) \\ \mathbf{W}_{vol} = \frac{1}{D_1} \kappa (J_{el} - 1)^2 \end{cases} \tag{12}$$

where \mathbf{I}_1 was the first isochoric invariants and \mathbf{I}_2 was the second isochoric invariants. And, D_1 was related to the bulk modulus κ , where $\kappa = 2/D_1$. The \mathbf{I}_1 and \mathbf{I}_2 were functions of the elastic right Cauchy-Green deformation tensors (\mathbf{C}). We assumed that the volume of the material was incompressible in the model. Then, $J_{el}(\text{volumetric deformation}) = 1$. Hence, the \mathbf{W}_{iso} equation in Eq. (12) could be removed.

Then, we attempted to obtain the two parameters of Mooney Rivlin model. Strain energy density and stress were usually expressed in the form of principal tensile ratio, $\lambda_a = L/L_0$ ($a = 1, 2, 3$), where L was the stretched length of the sample and the L_0 was the original length of the sample.

In uniaxial stretching, when $J = 1$, we have Eqs. (13) and (14):

$$\lambda_1 = \lambda, \lambda_2 = \lambda_3 = \frac{1}{\sqrt{\lambda}} \tag{13}$$

$$\mathbf{F} = \begin{pmatrix} \lambda & 0 & 0 \\ 0 & \frac{1}{\sqrt{\lambda}} & 0 \\ 0 & 0 & \frac{1}{\sqrt{\lambda}} \end{pmatrix} \tag{14}$$

So, we calculated the isochoric invariants \mathbf{I} by Eq. (15):

$$\begin{cases} \mathbf{I}_1 = (\lambda^2 + \frac{2}{\lambda}) \\ \mathbf{I}_2 = (2\lambda + \frac{1}{\lambda^2}) \end{cases} \tag{15}$$

And, in biaxial stretching, when $J = 1$, we have Eqs. (16) and (17):

$$\lambda_1 = \lambda_2 = \lambda, \lambda_3 = \frac{1}{\lambda^2} \tag{16}$$

$$\mathbf{F} = \begin{pmatrix} \lambda & 0 & 0 \\ 0 & \frac{1}{\sqrt{\lambda}} & 0 \\ 0 & 0 & \frac{1}{\sqrt{\lambda}} \end{pmatrix} \tag{17}$$

So, we calculated the isochoric invariants \mathbf{I} by Eq. (18):

$$\begin{cases} \mathbf{I}_1 = (2\lambda^2 + \frac{1}{\lambda^3}) \\ \mathbf{I}_2 = (\lambda^4 + \frac{2}{\lambda^2}) \end{cases} \tag{18}$$

Finally, we integrated the two formulas from uniaxial stretching and biaxial stretching and obtained Eq. (19):

$$\begin{cases} \sigma_{\text{trueuniaxial}} = \lambda \mathbf{P}_{1,\text{uniaxial}} = 2(\lambda^2 - \lambda^{-1})(C_{10} + \frac{C_{01}}{\lambda}) \\ \sigma_{\text{truebiaxial}} = \lambda \mathbf{P}_{1,\text{biaxial}} = 2(\lambda^2 - \lambda^{-4})(C_{10} + \lambda^2 C_{01}) \end{cases} \quad (19)$$

Where, \mathbf{P}_1 was the first Piola-Kirchhoff stress and $\mathbf{P}_1 = \mathbf{F}\mathbf{S}$.

We can get σ_{true} via the data of λ and $\mathbf{P}_1 = \sigma_{\text{engineer}}$ which were obtained from uniaxial stretching and biaxial stretching experiments. And then C_{10} and C_{01} could be calculated according to Eq. (19). Also, we can establish the bridge between material model and Eq. (7) based on the relationship above and conduct subsequent calculation and analysis.

For 3D model. In order to study the deformation and stress of an elastomer under certain compression depth conditions, we must give a pretension to the elastomer and set the contact between copper wire and elastomer. However, it is difficult to acquire a good convergence of the calculation under biaxial tension. Consequently, one end of the elastomer should be fixed. Then a time-varying loading is applied at another end of the elastomer. Finally, when the loading drops to zero and the von Mises stress are almost unchanged, we can use the calculation results for next analysis by Eq. (20) (also see Supplementary Fig. 12):

$$\begin{cases} \mathbf{u}(0, 0, z, t) = 0 \\ t = 0; \mathbf{u}_t(0, 0, l_p, t) = \mathbf{F}_p(x, y, z, t) \\ \frac{\partial F_p}{\partial z} = \mathbf{F}_p(t); \frac{\partial F_p}{\partial x} = \frac{\partial F_p}{\partial y} = 0 \end{cases} \quad (20)$$

For 2D model. Like 3D model, the deformation and stress of an elastomer under certain compression depth conditions were also studied in the 2D model. However, apart from the above, we paid more attention to the size of the area where the stress is larger than a certain value in the cross-section of the elastomer. It needs to be emphasized that the cross-section is perpendicular to the spiral of copper wire. We set a contact between copper and elastomer and give a speed for copper to reach a displacement as large as the depth. Then the bottom of the elastomer was fixed and a contact is set with the bottom line, so that the calculations converge more easily. Finally, when the displacement of copper meets the demand, we can use the calculation results for next analysis by Eq. (21) (also see Supplementary Fig. 13):

$$\begin{cases} \mathbf{u}(x, 0) = 0 \\ t = 0; \mathbf{u}_t(x, 0, y) = \mathbf{v} \end{cases} \quad (21)$$

Geometric and material parameters of the model are listed in Supplementary Table 4.

In a word, using the two-parameter Mooney-Rivlin model, we could introduce nonlinear mechanical behavior of eco-flex into the equilibrium equation of solid mechanics, and calculated the stress and strain of eco-flex at any time. Afterward, we studied the stress on eco-flex surface and restricted area under the tightening of copper wire.

Data availability

The data that support the findings of this study are available from the corresponding author upon request.

Received: 8 December 2022; Accepted: 18 April 2023;

Published online: 29 April 2023

References

- Gao, Y. et al. Winding-locked carbon nanotubes/polymer nanofibers helical yarn for ultrastretchable conductor and strain sensor. *ACS Nano* **14**, 3442–3450 (2020).
- Wang, H. et al. Superelastic wire-shaped supercapacitor sustaining 850% tensile strain based on carbon nanotube@graphene fiber. *Nano Res.* **11**, 2347–2356 (2018).
- Zhang, D. et al. Abrasion resistant/waterproof stretchable triboelectric yarns based on fermat spirals. *Adv. Mater.* **33**, 2100782 (2021).
- Yamamoto, Y. et al. Entropic and energetic elasticities of natural rubber with a nanomatrix structure. *Langmuir* **36**, 11341–11348 (2020).
- Gusev, A. A. & Schwarz, F. Molecular dynamics validation and applications of the maximum entropy homogenization procedure for predicting the elastic properties of gaussian polymer networks. *Macromolecules* **52**, 9445–9455 (2019).
- Hansoge, N. K. & Keten, S. Effect of polymer chemistry on chain conformations in hairy nanoparticle assemblies. *ACS Macro Lett* **8**, 1209–1215 (2019).
- De Rosa, C. et al. Mechanical properties and elastic behavior of high-molecular-weight poorly syndiotactic polypropylene. *Macromolecules* **36**, 7607–7617 (2003).
- Qiao, X. Y. et al. The crystallization and rheological behaviors of the ultrahigh molecular weight polyethylene swollen by petrolatum. *Polym Test* **80**, 106115 (2019).
- Patel, V. et al. Characterization of co- and post-hydrolyzed polyacrylamide molecular weight and radius distribution under saline environment. *J. Appl. Polym. Sci.* **138**, 50616 (2021).
- George, K. L. & Horne, W. S. Foldamer tertiary structure through sequence-guided protein backbone alteration. *Acc Chem. Res.* **51**, 1220–1228 (2018).
- Chaurasia, P. et al. Bent conformation of a backbone pilin N-terminal domain supports a three-stage pilus assembly mechanism. *Commun. Biol.* **1**, 94 (2018).
- Maeda, S. et al. Structure and selectivity engineering of the M1 muscarinic receptor toxin complex. *Science* **369**, 161–167 (2020).
- Chen, Q. et al. Structures of rhodopsin in complex with G-protein-coupled receptor kinase 1. *Nature* **595**, 600–605 (2021).
- Wegst, U. G. et al. Bioinspired structural materials. *Nat. Mater.* **14**, 23–36 (2015).
- Lee, T.-U. et al. Bending-active kirigami. *Int. J. Solids Struct.* **254–255**, 111864 (2022).
- Gao, J. et al. Kirigami nanofluidics. *Mater. Chem. Front.* **2**, 475–482 (2018).
- Yang, Y. et al. Grasping with Kirigami shells. *Sci. Robot.* **6**, eabd6426 (2021).
- An, N. et al. Programmable hierarchical Kirigami. *Adv. Funct. Mater.* **30**, 1906711 (2020).
- Cui, I. X. et al. Origami/Kirigami-guided morphing of composite sheets. *Adv. Funct. Mater.* **28**, 1802768 (2018).
- Alderete, N. A. et al. Machine learning assisted design of shape-programmable 3D kirigami metamaterials. *npj Comput. Mater.* **8**, 191 (2022).
- Guan, Y. S. et al. Kirigami-inspired nanoconfined polymer conducting nanosheets with 2000% stretchability. *Adv. Mater.* **30**, e1706390 (2018).
- Xu, L. et al. Origami and Kirigami nanocomposites. *ACS Nano* **11**, 7587–7599 (2017).
- Morikawa, Y. et al. Ultrastretchable Kirigami bioprobes. *Adv. Healthc. Mater.* **7**, 1701100 (2018).
- Teleki, A. & Artursson, P. Getting a grip with kirigami. *Nat. Mater.* **20**, 1043–1044 (2021).
- Shyu, T. C. et al. A Kirigami approach to engineering elasticity in nanocomposites through patterned defects. *Nat. Mater.* **14**, 785–789 (2015).
- Blees, M. K. et al. Graphene Kirigami. *Nature* **524**, 204–207 (2015).
- Hong, Y. et al. Boundary curvature guided programmable shape-morphing kirigami sheets. *Nat. Commun.* **13**, 530 (2022).
- Sorrentino, A. et al. Bio-inspired auxetic mechanical metamaterials evolved from rotating squares unit. *Mech. Mater.* **173**, 104421 (2022).
- Zou, S. B. et al. Spiderweb-inspired, transparent, impact-absorbing composite. *Cell Rep. Phys. Sci.* **1**, 100240 (2020).
- Wang, R. et al. Torsional refrigeration by twisted, coiled, and supercoiled fibers. *Science* **366**, 216–221 (2019).
- Song, Z. et al. Origami lithium-ion batteries. *Nat. Commun.* **5**, 3140 (2014).
- Wright, J. R. et al. Tensile properties of helical auxetic structures: a numerical study. *J. Appl. Phys.* **108**, 044905–044905 (2010).
- Wright, J. R. et al. On the design and characterisation of low-stiffness auxetic yarns and fabrics. *Text Res. J.* **82**, 645–654 (2012).
- Bhattacharya, S. et al. The variation in Poisson's ratio caused by interactions between core and wrap in helical composite auxetic yarns. *Compos. Sci. Technol.* **102**, 87–93 (2014).
- Zhang, G. H. et al. Varying the performance of helical auxetic yarns by altering component properties and geometry. *Compos. Struct.* **140**, 369–377 (2016).
- Sloan, M. R. et al. The helical auxetic yarn—a novel structure for composites and textiles; geometry, manufacture and mechanical properties. *Mech. Mater.* **43**, 476–486 (2011).
- Sorrentino, A. & Castagnetti, D. Negative Poisson's ratio lattice for designing vertebral biomaterials. *Mech. Adv. Mater. Struct.* **1–8** (2021).
- Neuefeind, J. et al. A multiple length scale description of the mechanism of elastomer stretching. *RSC Adv.* **6**, 95910–95919 (2016).
- Liu, S. et al. Study on the tensile behavior of helical auxetic yarns by modeling and mechanical analysis. *J. Textile Inst.* **112**, 1531–1537 (2021).
- Zheng, Y. et al. Indentation of a stretched elastomer. *J. Mech. Phys. Solids* **107**, 145–159 (2017).
- Liang, X. D. et al. Indentation of a prestretched strain-stiffening elastomer. *Math. Mech. Solids* **25**, 2118–2131 (2020).
- Ge, H. et al. How much force is needed to stretch a coiled chain in solution? *Macromolecules* **42**, 4400–4402 (2009).
- Marion, J. S. et al. Thermally drawn highly conductive fibers with controlled elasticity. *Adv. Mater.* **34**, 2201081 (2022).
- Ma, Z. et al. A superconducting-material-based maglev generator used for outer-space. *Adv. Mater.* **34**, 2203814 (2022).
- Zhang, X. et al. 3D-printed superhydrophobic and magnetic device that can self-powered sense a tiny droplet impact. *Engineering* **15**, 196–205 (2022).
- Liu, Z. et al. Multimaterial additive manufacturing manipulator for fabricating magnetoelectric pressure sensors. *Sci. China Technol. Sci.* **65**, 2542–2550 (2022).

47. Mooney, M. A theory of large elastic deformation. *J. Appl. Phys.* **11**, 582–592 (1940).

Acknowledgements

The authors would like to thank the financial support from the National Natural Science Foundation of China (grant No. 52125301 and 52203123) and the Fundamental Research Funds for the Central Universities. The research was partially sponsored by the Double First-Class Construction Funds of Sichuan University.

Author contributions

D.L. and Z.W.Z. equally contributed to this work, and led the experiments and the data collection; Z.Y.Z. and Y.J. contributed to the investigations, data analysis, and drawing of the schematics; Y.W. led the conceptualization, the methodology, and supervised the investigations; Y.W., X.F., W.Y., and Z.F.L. contributed to the methodology and funding acquisition; D.L. and Z.W.Z. led the writing of the original manuscript; Y.W., W.Y., and X.F. contributed to the writing. All authors contributed to the review and editing of the manuscript.

Competing interests

The authors declare no competing interests.

Additional information

Supplementary information The online version contains supplementary material available at <https://doi.org/10.1038/s43246-023-00355-6>.

Correspondence and requests for materials should be addressed to Xuewei Fu, Zunfeng Liu, Wei Yang or Yu Wang.

Peer review information *Communications Materials* thanks Zhuangjian Liu and the other, anonymous, reviewer(s) for their contribution to the peer review of this work. Primary Handling Editors: Jet-Sing Lee and Aldo Isidori. Peer reviewer reports are available.

Reprints and permission information is available at <http://www.nature.com/reprints>

Publisher's note Springer Nature remains neutral with regard to jurisdictional claims in published maps and institutional affiliations.



Open Access This article is licensed under a Creative Commons Attribution 4.0 International License, which permits use, sharing, adaptation, distribution and reproduction in any medium or format, as long as you give appropriate credit to the original author(s) and the source, provide a link to the Creative Commons license, and indicate if changes were made. The images or other third party material in this article are included in the article's Creative Commons license, unless indicated otherwise in a credit line to the material. If material is not included in the article's Creative Commons license and your intended use is not permitted by statutory regulation or exceeds the permitted use, you will need to obtain permission directly from the copyright holder. To view a copy of this license, visit <http://creativecommons.org/licenses/by/4.0/>.

© The Author(s) 2023